

# Scanning Transmission Electron Microscopy and Related Techniques for Research on Actinide and Radionuclide Nanomaterials

Satoshi Utsunomiya, Masashi Kogawa, Eigo Kamiishi, and Rodney C. Ewing

**Abstract** The physical and chemical properties of actinide-bearing materials, as well as other radionuclides, such as fission product elements from the nuclear fuel cycle, depend greatly on their electronic configuration, crystal structure, thermochemical parameters, and the amount of impurity elements at the atomic scale. Further, nanoscale particles may have distinctly different properties from the bulk composition. In order to understand the properties of such materials, direct characterization at the nanoscale is essential. This chapter reviews relevant methods for direct analysis of nanoscale materials using a focused electron beam, scanning transmission electron microscopy (STEM), in which the electron probe can be less than an Å size with the current high enough to perform elemental analysis. High-angle annular dark-field STEM (HAADF-STEM) provides an incoherent image by which the intensity correlates with the atomic number. The HAADF-STEM image can be greatly enhanced by a theoretical filtering method, such as the maximum entropy method. Electron energy-loss spectroscopy (EELS) allows the investigation of the chemical state including oxidation state and the electron density of states at the nanoscale. Three dimensional electron tomography with STEM or TEM imaging is another useful method for obtaining morphological and topological information of nanoscale materials. In addition, the recent development of the aberration corrector for spherical aberration ( $C_s$ ) has achieved a sub-Å probe as small as  $\sim 0.5$  Å in STEM, which greatly improves the spatial resolution of images and chemical analyses. The application of  $C_s$ -corrected STEM has not been explored in actinide research; however, it has great potential in the investigation of the properties of actinide materials at the atomic-level.

---

S. Utsunomiya (✉), M. Kogawa, and E. Kamiishi  
Department of Chemistry, Kyushu University, 6-10-1 Hakozaki, Higashi-ku, Fukuoka 812-8581,  
Japan  
e-mail: utu@chem.rc.kyushu-u.ac.jp

R.C. Ewing  
Department of Geological Sciences, University of Michigan, Ann Arbor 48109-1005, MI, USA

## 1 Introduction

Detailed characterization of nanoscale materials – their structure, composition, and chemical state – is essential for the evaluation of their physical and chemical properties. One of the most powerful methods for obtaining such information is by the use of transmission electron microscopy (TEM). Conventional TEM (CTEM) including analytical electron microscopy (AEM) and high-resolution TEM have been widely used. Indeed, for actinide research, early TEM and scanning TEM (STEM) studies already provided important knowledge about alteration of nuclear waste glass (e.g., [1–4]) and fission products in spent nuclear fuel (e.g., [5]). The fundamentals of basic CTEM are described in many text books (e.g., [6, 7]); thus, this chapter will not cover CTEM. Rather, this paper reviews various aspects in STEM, because the focused probe is a powerful means for determining both the local composition and the chemical state by using an energy dispersive X-ray spectroscopy (EDS) and an electron energy-loss spectroscopy (EELS) at a spot size that is near the atomic scale. With an HAADF detector, STEM is capable of incoherent imaging that reveals the chemical composition. The combination of HAADF-STEM with EDS or EELS is a very useful method for describing the heterogeneous distribution of radionuclides; and thus, it has been applied to the characterization of nuclear materials, which are summarized in this chapter. In addition, the size of STEM probe has been dramatically improved in the recent several years owing to the application of the spherical aberration ( $C_s$ ) corrector to STEM. The other capability that is described is tomography, which allows three dimensional visualization of nanoscale materials. These two imaging methods are also reviewed in this chapter.

## 2 HAADF-STEM

### 2.1 *Comparison of HAADF-STEM with Conventional TEM*

Although HRTEM and the associated analytical capabilities are generally the most appropriate techniques for investigating the structural and chemical properties of nanoscale particles, the amount of the sample that is actually examined is extremely limited due to the high resolution in TEM. This is an important limitation when the element of interest is sparsely distributed and at low concentrations, particularly because the contrast in CTEM is formed by a coherent imaging process. Even though the atomic scattering factor is greater for the heavy elements, such as actinides, and those atoms appear ideally as darker spots (Fig. 1a, top), the contrast transfer function (CTF) varies as a function of objective lens defocus and the specimen thickness when forming the coherent image in high resolution phase contrast imaging. Hence, it is not the easiest

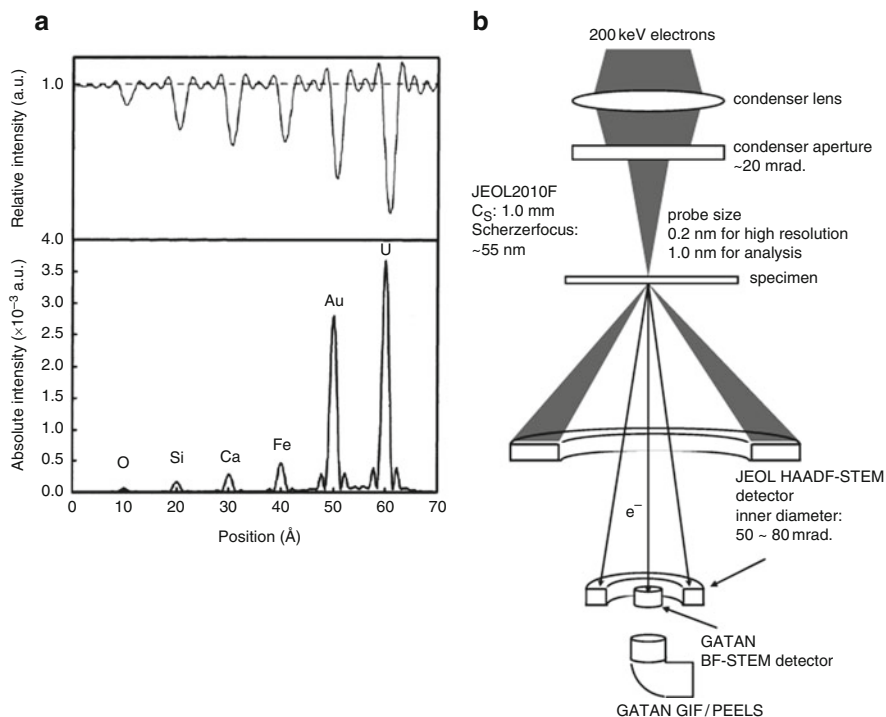


**Fig. 1** (a) Simulated contrast profile calculated for each atom of each element discussed in the examples of this study. The calculation was completed using the code developed by Kirkland [8]. The atoms were placed in a row at 1-nm intervals. (top) BF-CTEM contrast profile. (bottom) HAADF-STEM contrast profile. (b) Schematic illustration of the electron microscope configuration used in the HAADF-STEM mode (JEOL JEM2010F). Both (a) and (b) were reproduced from Utsunomiya and Ewing [9]

approach to observe actinides at very low concentrations. Bright-field (BF) images in the STEM mode are formed by a coherent process, essentially the same as BFTEM at high resolution; whereas, STEM turns into a remarkably powerful method when electrons are collected by a high-angle annular detector. Figure 1 shows the configuration of an electron microscope in the HAADF-STEM mode. When the particle consists of relatively heavy elements, as compared to the composition of the matrix material, HAADF-STEM becomes useful for finding the nanoparticles of interest, as the contrast of the image is strongly correlated with atomic number and sample thickness. For example, a contrast profile calculated for each atom with various  $Z$  numbers based on the multislice method is illustrated in Fig. 1a (bottom), which clearly reveals a positive correlation of the contrast in HAADF-STEM with  $Z$ . The power of the derived  $Z$  dependence of the intensity generally ranges 1.5–1.8; that is, the intensity  $\propto Z^{1.5-1.8}$  [10].

## 2.2 Development in HAADF-STEM

As one can easily imagine, the early studies using annular dark-field (ADF)-STEM were dedicated to imaging various heavy atoms on the surface of a thin film of carbon, and interestingly, the selected targets included U acetate, organic matter with U dimer, and U chloride [11, 12]. It was already realized in those days that, given an appropriate geometry for the annular detector, elastically scattered electrons at large angle (50–100 mrad) form an image with negligible phase-contrast effects. In the late 1980s and the early 1990s, HAADF-STEM was under active development, particularly for obtaining near-atomic scale chemical imaging of inorganic crystals in material science; for example, Pt catalyst clusters [13], ion-implanted Si [14], superconductor material,  $\text{YBa}_2\text{Cu}_3\text{O}_{7-\delta}$  [15, 16]. Unlike CTEM, HAADF-STEM is based on the incoherent imaging process, and the contrast of the image is not reversed by defocusing or by the specimen thickness [17, 18]. A theoretical study noted that the intensity in HAADF-STEM can vary slightly as a function of specimen thickness due to contributions from coherent and multiple scattering [19].

Thermal diffuse scattering (TDS), which is a signal used to form the image in HAADF-STEM and which was previously considered as “background intensity,” became a powerful source of information by using an HAADF detector. According to Kirkland [8], fundamentally, each atom in the specimen vibrates thermally with a frequency of  $10^{12}$ – $10^{13}$  Hz. The atomic vibration is quantized, and the quantum unit is a “phonon”. The electron’s velocity in the beam of the electron microscope is approximately  $1.5 \times 10^{10}$  cm/s. Thus, the time required for the electron to pass through the specimen is approximately  $0.7 \times 10^{-16}$  s, which is much shorter than the oscillation period of the atoms. However, the period between successive electrons in an incident electron beam is longer than that of atomic oscillations. Therefore, the image of each configuration of atoms is unique due to the random atomic oscillations; as a result, the average of all the configurations of atoms eventually becomes incoherent. The TDS profile through spatial frequency can be calculated by the “frozen phonon” method, in which the atoms are allowed to deviate from their original position following a Gaussian distribution [20].

## 2.3 Basic Imaging Theory in HAADF-STEM

The fundamental physics of the HAADF-STEM are described following Kirkland [8]. The wave function of a focused probe at a position,  $\mathbf{x}_p$ , is expressed as an integration of the aberration wave function over the objective aperture (aperture size is  $\alpha_{\max}$  in maximum angle):

$$\psi_p(\mathbf{x}, \mathbf{x}_p) = A_p \int_0^{k_{\max}} \exp[-i\chi(\mathbf{k}) - 2\pi i\mathbf{k}(\mathbf{x} - \mathbf{x}_p)] d\mathbf{k} \quad (1)$$

$$\lambda k_{\max} = \alpha_{\max} \quad (2)$$

where  $\chi(k)$  is the aberration function,  $\lambda$  is the wavelength of the electron, and  $A_p$  is a normalization factor to produce:

$$\int |\psi_p(\mathbf{x}, \mathbf{x}_p)|^2 d\mathbf{x} = 1 \quad (3)$$

The transmission function of the specimen is:

$$t(\mathbf{x}) = \exp[i\sigma v_z(\mathbf{x})] \quad (4)$$

Here,  $\sigma$  is an interaction parameter expressed as:

$$\sigma = \frac{2\pi}{\lambda V} \left( \frac{m_0 c^2 + eV}{2m_0 c^2 + eV} \right) \quad (5)$$

where  $m_0$ ,  $c$ , and  $eV$  are the rest mass of the electron, the speed of light in vacuum, and the kinetic energy of the electron in vacuum, respectively. The  $v_z(\mathbf{x})$  in (4) is the projected atomic potential of the specimen. The resulting transmitted wave function is:

$$\Psi_t(\mathbf{x}) = t(\mathbf{x})\psi_p(\mathbf{x}, \mathbf{x}_p) \quad (6)$$

Finally, the wave function on the diffraction plane can be described as:

$$\Psi_t(\mathbf{k}) = FT(\psi_t(\mathbf{x})) \quad (7)$$

The signal on HAADF detector,  $g(\mathbf{x}_p)$ , is the integration of intensity on the detector:

$$g(\mathbf{x}_p) = \int D(\mathbf{k}) |\Psi_t(\mathbf{k})|^2 d\mathbf{k} \quad (8)$$

$$\begin{aligned} D(k) &= 1 \quad \text{on the detector} \\ &= 0 \quad \text{outside of the detector.} \end{aligned} \quad (9)$$

As expected from (1), (7), and (8), a convergent-beam diffraction pattern is formed on the back-focal plane. Thus, the intensity on the detector is the sum of the pure elastic scattered electrons and the pure TDS electrons. Because the elastic scattering must satisfy Black's condition, that is the reciprocal lattice must cross Ewald's sphere, the intensity of zero order Laue zone (ZOLZ) becomes weak and disappears in the high-frequency region of the diffraction space. As a result, TDS scattering becomes dominant at high angles and is recorded by the HAADF

detector. However, the first order or high order Laue zone (FOLZ or HOLZ) is possible, and this signal may also be recorded by the HAADF detector. Eventually, the contrast of the HAADF image is a result of the relative intensities of elastic scattering and TDS on the HAADF detector.

## ***2.4 Image Simulation and Filtering for HAADF-STEM***

To simulate the high resolution HAADF-STEM image, Bethe's eigenvalue method [18, 21] and the multislice method [22–24] have been employed. An advantage of the multislice method is its ability to account for mixed layers in the calculation of specimen potential, which is performed by a linear superposition of the atomic potential of each atom in the specimen; the atomic potential is related to the scattering factor.

McGibbon et al. [25] demonstrated significant enhancement in the quality of the Z-contrast image by using the maximum entropy analysis. The image intensity is generally described by a deconvolution between a point spread function and an object function, and the authors applied the technique of maximum entropy [26, 27] in order to obtain the sharpest “most likely” object function resulting in decrease of the image noise and to locate the atomic column positions with an accuracy of approximately 0.02 nm. This method leads to the much improved atomic-scale Z-contrast imaging coupled with  $C_s$ -corrected STEM [28], which is described in a later section.

## ***2.5 Application of HAADF-STEM to Nuclear Materials***

The HAADF-STEM study has not been widely employed in radiological sciences as compared with numerous applications reported in materials science. In this section, we first describe examples of HAADF-STEM applied to uranium nanoparticles in various environments and then discuss topics relevant to nuclear materials.

### ***2.5.1 Uranium in Atmosphere***

The occurrence of toxic metals including actinides in the ambient atmosphere is a critical environmental issue. In particular, those metals in fine fraction (PM<sub>2.5</sub>) can have increased toxicity and most likely penetrate deep into the respiratory system. Utsunomiya et al. [29] performed chemical and structural characterization of individual fine atmospheric particulates collected from Detroit urban area utilizing HAADF-STEM in addition to bulk analysis. Among many heavy metals, the authors found particles with extremely high contrast in HAADF-STEM image,

which mainly consist of U and O (Fig. 2a). In this sample, the U concentration was determined to be  $0.25 \text{ ng/m}^3$  (9.2 ppm) prior to the TEM investigation by bulk analysis. This work demonstrated that even actinides existing at the very low concentrations can be detected efficiently by means of HAADF-STEM. Interestingly, some of the nanocrystals of uraninite were completely encapsulated by a fulleroid (Fig. 2b). In this “fulleroid shell,” the U appears to be partially protected from the ambient oxidizing conditions of the atmosphere, and this reduces its mobility in the environment, as oxidized species of uranium are highly mobile. Rigorous characterization of U in the atmospheric particulates is directly linked to its bioavailability and also provides new insight into the transportation processes of uranium by aerosols.

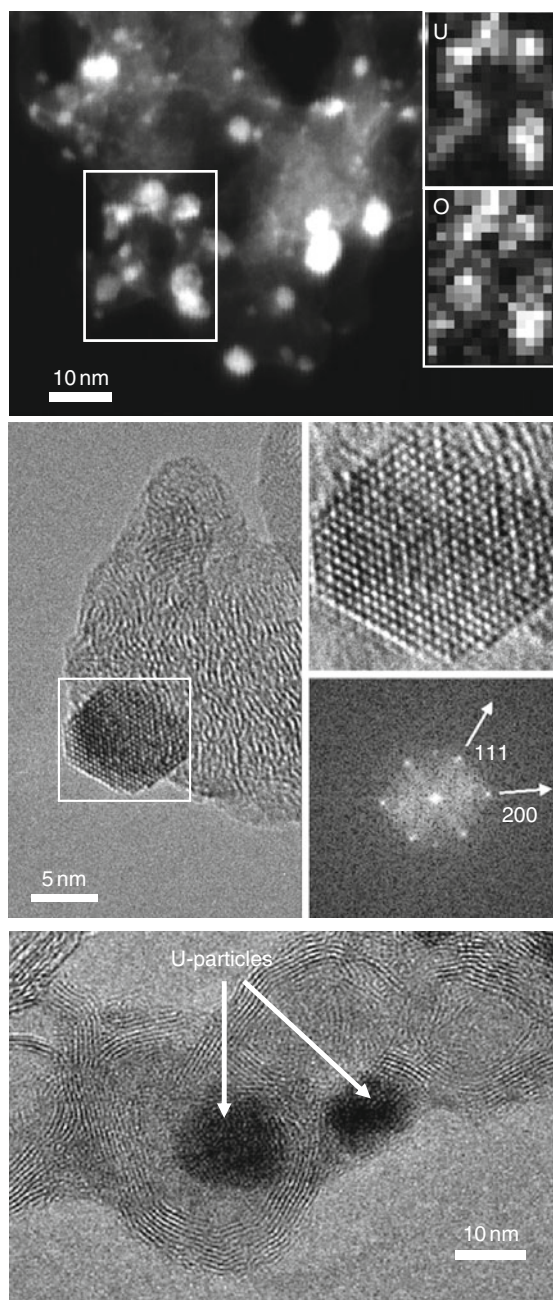
### 2.5.2 Uranium Precipitates on the Bacteria

Uranium can be utilized by microbes [30–33], which take advantage of the multiple oxidation states of U(IV and VI) as a source of energy. The use of STEM was not common in this research topic because the experiments were well controlled, and CTEM usually provided the essential data for the characterization of the nanoparticles formed on the surface of bacteria. Fayek et al. [34] demonstrated the value of the coupled analyses of HAADF-STEM and nano-SIMS to characterize U nanoparticles formed on the cell surface. In their study, a *Geobacter sulfurreducens* biofilm was placed in contact with  $\text{U}^{6+}$ -rich synthetic groundwater. It is obvious that the HAADF-STEM images shown in Fig. 3 generally provide information of U localization both in large and small areas of observation. The associated EDS elemental maps confirm the U distribution that is approximately correlated with the distribution of high contrast spots, although the mapping takes as long as ~1 h, and the X-ray count at low concentrations is often not distinguishable from background counts due to the short dwell time per pixel. Hence, HAADF-STEM imaging is helpful to quickly determine the location of the U at a scale <10 nm. These U precipitates were subsequently characterized as uraninite,  $\text{UO}_{2+x}$ , which were also observed in the previous study [33].

### 2.5.3 Submicron Scale Phenomena in Uraninite and Coffinite Alteration

Natural U ore deposits mainly consist of uraninite,  $\text{UO}_{2+x}$ , and this provides a great opportunity for the investigation of the process of uraninite alteration over geologic time scales, specifically reflecting the regional mineralogy, the physico-chemical conditions of the fluid, and the age of formation of the U-ore. Because uraninite alteration process in nature can provide an important insight that is applicable to the safe geological disposal of U-bearing nuclear waste, many previous studies have reported bulk and microscopic phenomena in several U deposits all over the world, which have already been summarized in a review article (e.g., [35]). On the other hand, there are limited studies that characterized alteration zone at the submicron scale. Recently, a HAADF-STEM has been successfully applied to

**Fig. 2** Application of HAADF-STEM to characterize uraninite nanoparticles in the atmospheric particulates [29] (a) BF-TEM image reveals the presence of small particles within the carbonaceous matter of the soot. (b) HAADF-STEM image of the area reveals the occurrence of many heavy particles less than 10 nm in size. The *insets* are elemental maps of uranium and oxygen by STEM-EDX. (c) HRTEM images show that U-bearing nanoparticles are encapsulated in the “cage” structure of fulleroid





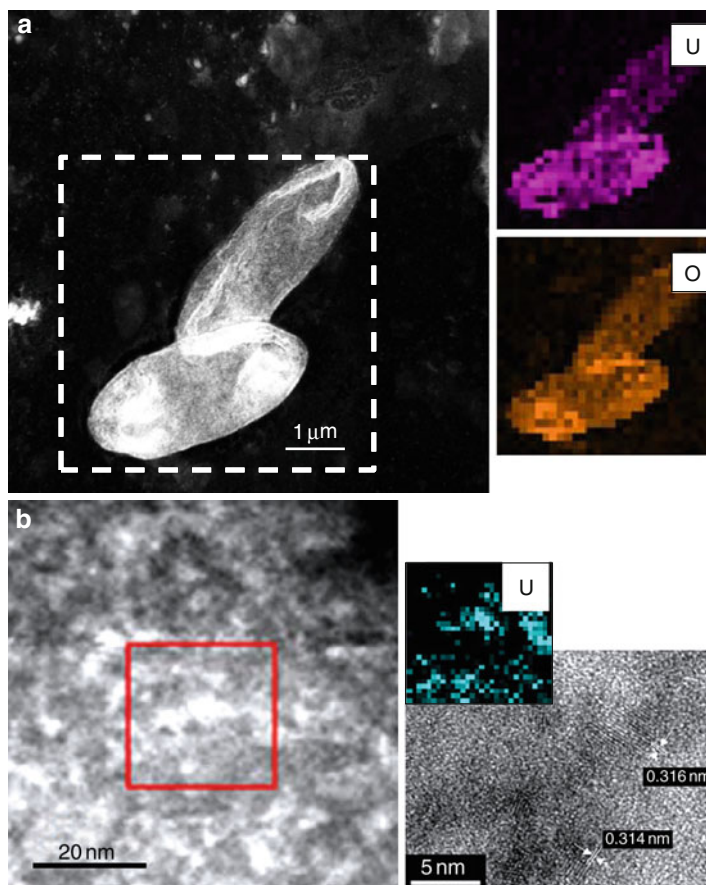


**Fig. 3** HAADF-STEM images of *Geobacter sulfurreducens* after contacting with U solution [34]. (a) Magnified image showing the whole bacteria. (b) STEM-EDX element-distribution maps of Na, Cl, O, and U showing these elements located on the surface of the bacteria. Red box represents area selected for high-resolution (nm) HAADF-STEM analysis shown in (b). (a) (b) HAADF-STEM image of the surface of bacteria (area outlined in red, Fig. 2). (b) STEM-EDX element-distribution maps of Na, Cl, O, and U from the region outlined in (a), showing the congruency between O and U, and Na and Cl. Note that U and Cl are decoupled. (c) HRTEM image showing the size of the nanocrystals of uranium oxide on the surface of the bacteria. Numbers are  $d$  values, which are indicative of the mineral uraninite ( $\text{UO}_2$ ). Samples were obtained from the 4-day experiments

investigate the alteration and precipitation of coffinite,  $\text{USiO}_4$  [36, 37], and coffinitization of uraninite [38]. For example, Fig. 4a–c display alteration front of coffinite in the presence of apatite. The sample was from the Woodrow Mine, Grants uranium region, New Mexico. The phase boundary and the dissolution pores were clearly evident even at the thicker parts of the specimen, while they are unambiguously displayed if observed by CTEM. Thus, it is emphasized that HAADF-STEM imaging is suitable for a relatively thick sample. Based on these

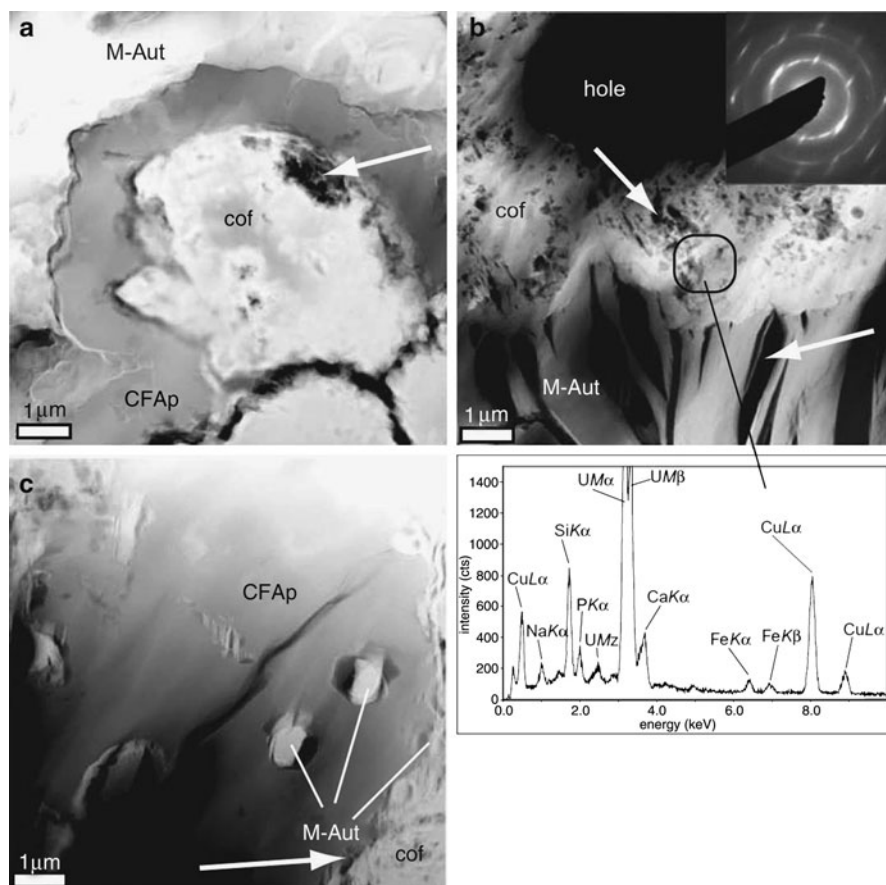


**Fig. 4** HAADF-STEM images of the associated coffinite, M-Aut and CFap [37]. (a) Dissolution of CFap by coffinite and subsequent alteration of coffinite and CFap to M-Aut; (b) Alteration of coffinite to M-Aut with associated SAED pattern of M-Aut and EDS analysis of the porous coffinite enriched with Na (*rimmed area*); the diffused diffraction maxima indicate a low crystallinity of precipitated M-Aut; (c) M-Aut precipitating inside CFap grains and at the interface between CFap and coffinite; (a)–(c) Note the extensive formation of porosity

data coupled with the results from electron microprobe, the authors concluded that microscale dissolution of apatite can create conditions conducive to the precipitation of U(IV)- and U(VI)-minerals, leading to the reduced mobility of U-species under both reducing and oxidizing conditions [37].

#### 2.5.4 Groundwater Colloids and Nanoscale Particles in the Contaminated Sites

Nanometer-sized colloids, consisting of inorganic and/or organic compounds, provide an important means of transporting elements with low solubilities, including

the actinides [39, 40]. The formation of actinide pseudo-colloids, in which the actinide sorbs onto aquatic colloids, can stabilize actinides in natural waters and increase their concentrations by many orders of magnitude over the values expected from solubility calculations [40, 41]. In spite of the numerous studies of colloids, there is still a lack of information on the speciation of the actinides or the type of colloids with which they are associated, particularly during the transport in the far-field, some kilometers from the source. At the Mayak Production Association, Urals, Russia, Pu was found to be associated with amorphous Fe-hydroxide (Fig. 5a and b) and was transported through the groundwater system [43]. Unfortunately, the HAADF-STEM was not able to capture the adsorbed Pu atoms on those colloids. It was also reported that Pu has migrated 1.3 km in 30 years in groundwater by means of colloids with sizes of 7 nm to 1 mm at Nevada Test Site [44]. In Utsunomiya et al. [42], a variety of radionuclides including U were identified in the same samples of Kersting Oet al. [44] from Nevada Test Site by a HAADF-STEM; cesium uranate, Co in Fe–Ni–Cr alloy, uranyl minerals (Na-boltwoodite and U oxide hydrates) (Fig. 5c–e). The presence of these colloids was not predicted considering the solubility of these phases, which may imply a thin coating layer on the surface of the colloids. Nonetheless, the phase-dependent transport of these elements is of critical importance, as each colloidal phase has characteristic properties in terms of mobility, under the specific physicochemical conditions of groundwater.

### 2.5.5 Uranium Cluster Formation on Muscovite

Arnold et al. [45] conducted U(VI) adsorption experiments onto muscovite at room temperature, and then the U speciation was examined by HAADF-STEM and time-resolved laser-induced fluorescence spectroscopy (TRLFS). Results from TRLFS indicated the presence of two adsorbed uranium(VI) surface species on edge-surfaces of muscovite with different coordination environments: On the other hand, HAADF-STEM revealed that nanoclusters of an amorphous uranium phase were attached to the edge-surfaces of muscovite. These U-nanoclusters were not observed on {001} cleavage planes of the muscovite. Combined with the TRLFS data, the two surface species were characterized as truly adsorbed bidentate surface complexes, in which the U(VI) binds to aluminol groups of edge-surfaces, and amorphous U(VI) condenses as nanosized clusters of polynuclear uranyl(VI) surface species with a particle diameter of 1–2 nm. Formation of these U nanoclusters on the edge of ferrous mica was also reported in Ilton et al. [46]. This example clearly demonstrates the successful combination of HAADF-STEM with another analytical method, in this case, TRLFS.

### 2.5.6 Applications to the Nuclear Materials

As a daughter nuclide in the decay chain, Pb is of critical importance in radiochemistry and geosciences. On the other hand, zircon ( $\text{ZrSiO}_4$ ) has been proposed as

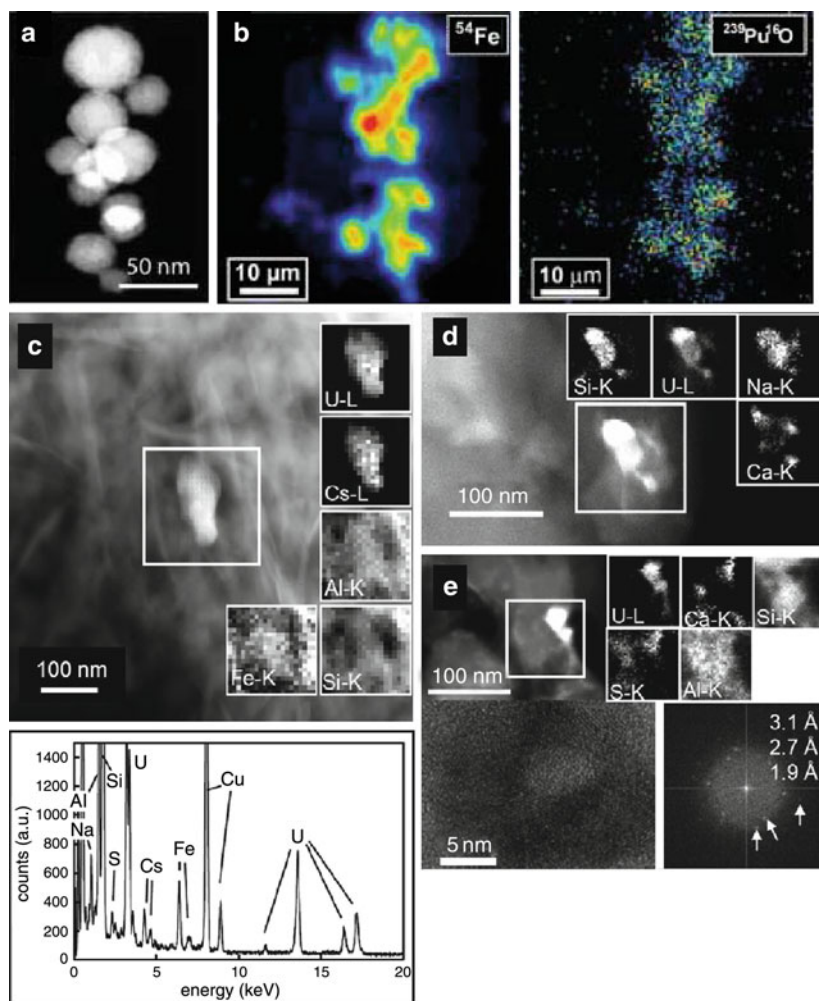


**Fig. 5** (a) HAADF-STEM image of the spherical colloids in the groundwater collected at the Mayak Production Association, Urals, Russia. (b) Nano-SIMS elemental maps of the colloids. (c) HAADF-STEM image of Cs–U-phase with the elemental maps. (d) EDX spectrum (*bottom*) of this Cs–U-particle. Cu-peak is from Cu-grid. HAADF-STEM image of Na-boltwoodite with elemental maps. (e) HAADF-STEM image with the elemental maps of U-phase attached to the zeolite surface. The HRTEM image (*bottom left*) of the U-phase accompanied by the indexed FFT image (*bottom right*) reveals the presence of uraninite nanocrystals after exposure to the electron beam in STEM mode [42]

a waste form for immobilization of Pu from dismantled nuclear weapons [47, 48]. Hence, loss of trace elements, e.g., U, Pb, and Pu, from zircon depends on the form of these elements and is of critical interest. Utsunomiya et al. [49] investigated a high concentration Pb-zone (0.03 wt%) in a natural zircon crystal from meta-sedimentary belt near the Jack Hills [50, 51] using HRTEM and HAADF-STEM.

A HAADF-STEM image revealed some patches of relatively high contrast, ~5 nm in the diameter (Fig. 6a), and the nanoscale elemental map revealed the high concentration of Pb (~3 wt%). The high resolution HAADF-STEM image of a Pb-rich region showed a continuous zircon structure without distortion across the Pb-rich region (Fig. 6b). It was suggested that (1) Pb substitutes directly for Zr in the zircon structure, and that (2) there is no other Pb-rich phase present.

In addition to the patchy occurrence of Pb, numerous fission tracks were observed in <5 nm width, which were created by high-energy (~100 MeV), heavy particles from spontaneous fission events (Fig. 6c). Although spontaneous fission of  $^{238}\text{U}$  is infrequent (decay constant =  $10^{-16}$  per year), the old age (>~3.3 Ga) and actinide content of these zircons suggests that fission tracks are to be expected. The majority of the fission tracks showed a dark contrast in the HAADF-STEM images; however, one fission track had a higher concentration of Pb (Fig. 6d) throughout the length of the entire track. The edge of the zircon lattice (Fig. 6e), indicated by a yellow arrow, shows a lattice image with higher contrast than the bulk zircon matrix, indicating the incorporation of Pb atoms into the zircon structure adjacent to the fission track. These results suggest that among many fission tracks and nanoscale Pb-rich domains, one Pb-rich domain was coincidentally cut across by a fission track, and Pb preferentially diffused along the amorphous track.

The advantage of HAADF-STEM with EDS mapping was also demonstrated in a study that characterized the metallic epsilon phase nanoparticles in the reactor zone 10 in Oklo natural fission reactor [52]. The epsilon phase (Mo–Ru–Pd–Tc–Rh) is an important host of  $^{99}\text{Tc}$  derived from a fission reaction, which has a long half life ( $2.13 \times 10^5$  years). HAADF-STEM images show an Ru–As particle ~300 nm in size surrounded by a Pb-rich region within the uraninite matrix (Fig. 7a). The composition of the particle was determined semiquantitatively as: As, 59.9; Co, 2.5; Ni, 5.2; Ru, 18.6; Th, 8.4; Pd, 3.1; Sb, 2.4 in atomic% (Fig. 7b). The Ru–As phase was not a single particle but an aggregate of 100–200 nm sized particles. The phase was identified as ruthenarsenite, (Ru, Ni)As, based on the HRTEM image and the FFT (fast Fourier transformed) image (Fig. 7c).

Another Ru-phase observed in this sample was 600–700 nm in size. The elemental distribution is rather complicated for this inclusion, as shown in the elemental maps (Fig. 7d). Lead occurs at the core of the particle; whereas, the rim of the inclusion consists of Ni, Co, and As without Ru. The Ru is enriched in the intermediate zone, associated with As and Ni, forming ruthenarsenite. This complexly mixed texture suggests that a process of dissolution and precipitation occurred within this inclusion. Based on the nanoscale characterization by HAADF-STEM combined with EDS and HRTEM, the history that the epsilon phases have experienced may be as follows (1) The original epsilon phase was changed to, in most cases, ruthenarsenite, by As-rich fluids with other trace metals. Dissolution and a simultaneous precipitation may be responsible for the phase change. (2) All Mo and most of the Tc were released from the epsilon phase. Galena precipitated surrounding the 4d-metal phases. (3) Once the uraninite matrix has dissolved, the epsilon nanoparticles were released and “captured” within alteration phases that are immediately adjacent to the uraninite.



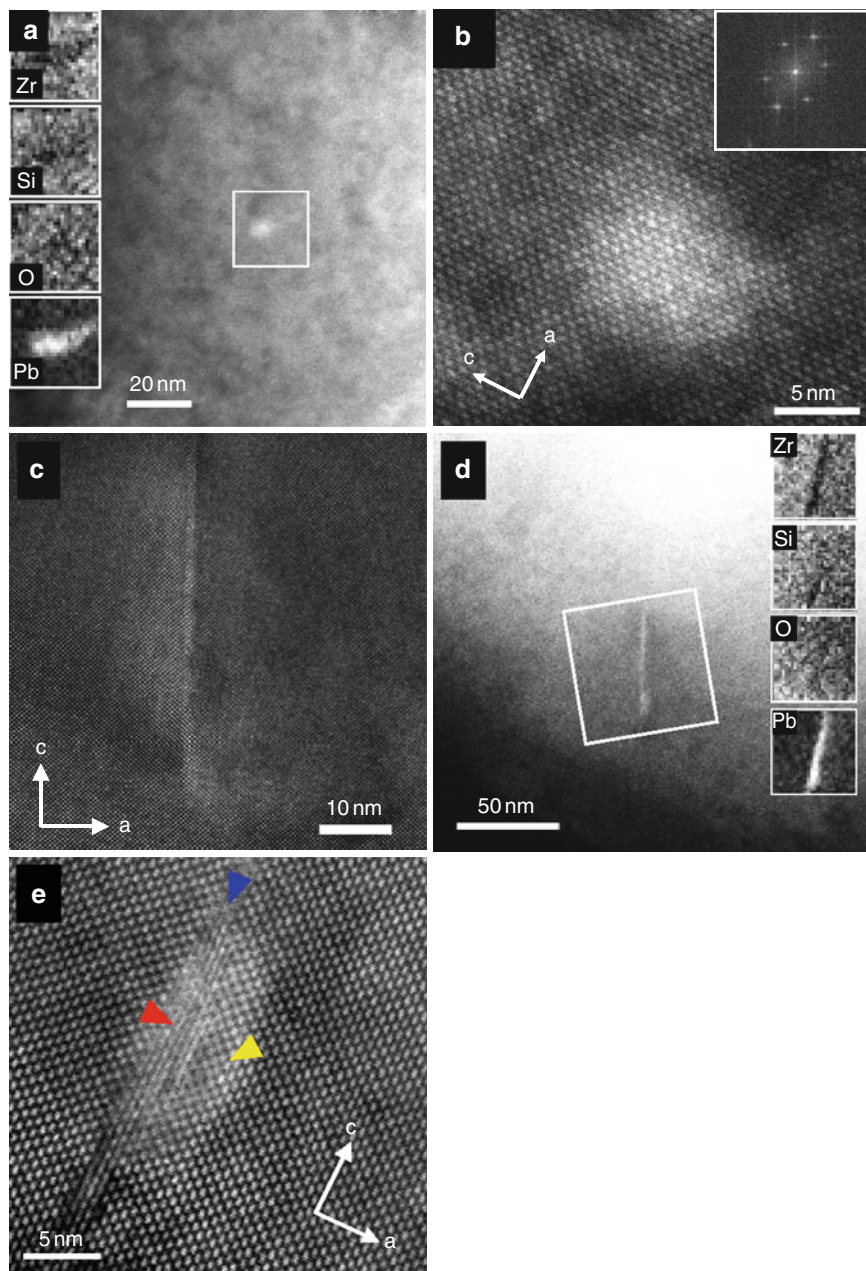


**Fig. 6** The occurrence of Pb in the Archean zircon [49]. (a) HAADF-STEM image of a patchy concentration of Pb in zircon associated with elemental maps of the *boxed region*. (b) High resolution HAADF-STEM image from the view along [010] with the *inset* of the FFT image. (c) HRTEM image of the fission track with the view along [010]. The direction of the fission track is parallel to the (010) plane. (d) HAADF-STEM image of the fission track with the elemental maps of the *boxed area*. (e) High resolution HAADF-STEM image of the fission track from the view along [010]

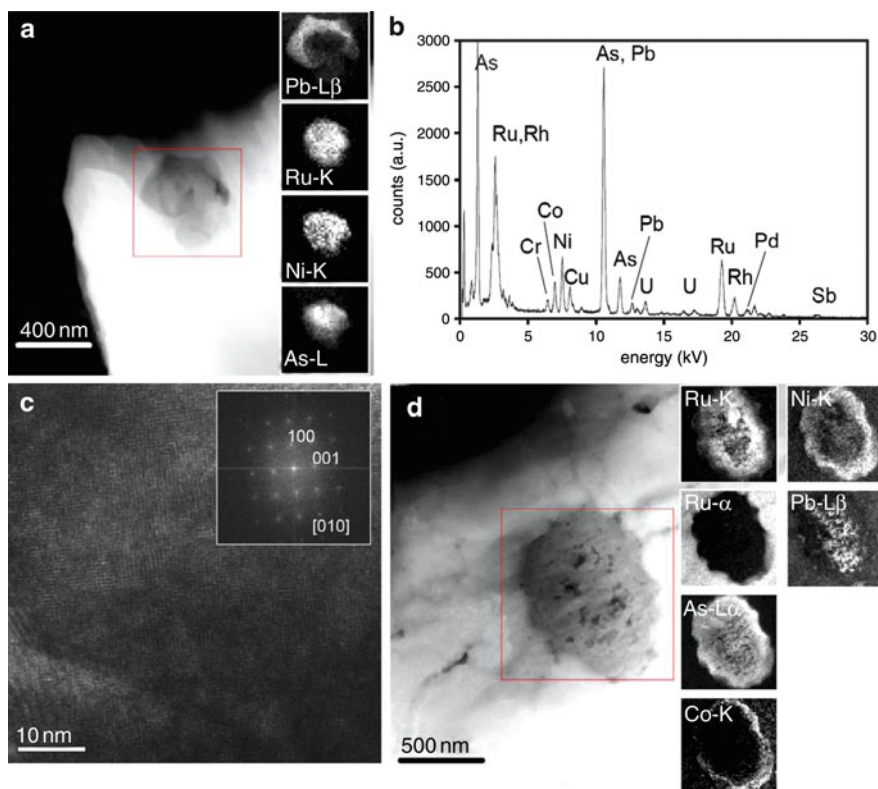


**Fig. 7** HAADF-STEM images (**a** and **d**) with EDS maps of the epsilon particles in the uraninite matrix in the reactor zone 10 of Oklo natural fission reactor [52]. (**a**) Ruthenarsenite nanoparticle, which was identified by the EDS spectrum (**b**) and the HRTEM with FFT image (**c**). (**d**) A Ru-phase mixed with the other metals; Ni, Co, As, and Pb

HAADF-STEM imaging was also employed to characterize ion-irradiated synthetic garnet structure that incorporates a variety of potential fission products [53]. Figure 8 shows the high resolution TEM (a) and HAADF-STEM image (b) of the garnet,  $(\text{Ca}_{2.37}\text{Th}_{0.56})^{\text{VIII}}(\text{Zr}_{2.03})^{\text{VI}}(\text{Fe}_{2.96})^{\text{IV}}\text{O}_{12}$ , which was irradiated by 1.0 MeV  $\text{Kr}^{2+}$  at 0.12 dpa (displacement per atom) at room temperature. In the HAADF-STEM image, amorphous domains appear as darker areas. As summarized in the previous section, there are some factors that can make the amorphous matrix have a darker contrast in the HAADF-STEM mode; thickness, density, structural configuration of specimen, and the average mass [9]. In this case, the chemical composition of the amorphous volume does not change significantly as compared to that of the crystalline remnants. Thickness and density in the amorphous domains possibly changed from the original garnet. The previous studies on radiation effects in zircon reported that swelling increases and the density decreases concurrently with the increasing accumulation of dose [54, 55]. The swelling may result in an increase of

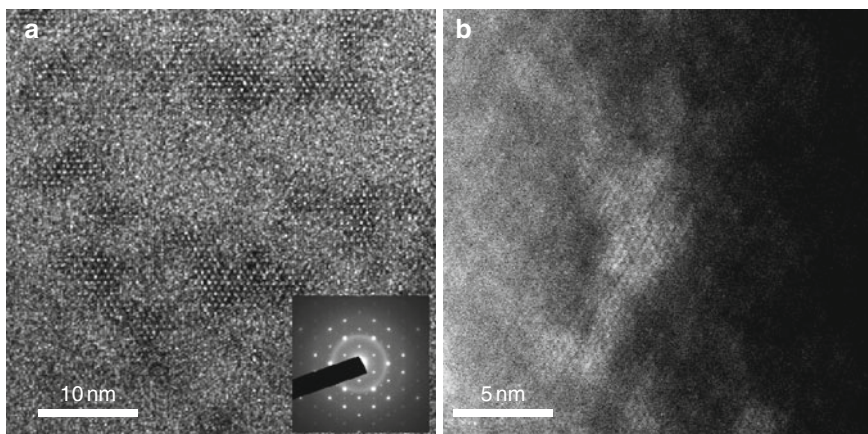


**Fig. 8** HRTEM image and HAADF-STEM image of the garnet  $(\text{Ca}_{2.37}\text{Th}_{0.56})^{\text{VIII}}(\text{Zr}_{2.03})^{\text{VI}}(\text{Fe}_{2.96})^{\text{IV}}\text{O}_{12}$ , after the irradiation with 1.0 MeV  $\text{Kr}^{2+}$  at 0.12 dpa (displacement per atom) at room temperature [53]

thickness in the amorphous area, and the thicker amorphous area may have a brighter contrast in HAADF-STEM, but the decrease of density in the amorphous area has an opposite contribution, making the contrast darker. A loss of the structural configuration in radiation-induced amorphous domain can also make the contrast darker as observed in zircon. Thus, the combined effect of the loss on the structural configuration and of the decrease on the density in the amorphous domains contributed to the contrast being greater than the effect of thickness changes.

Xenon is also one of the fissiogenic elements in nuclear reaction. Mitsuishi et al. [56] performed atomic-scale HAADF-STEM imaging of Xe in Al metal combined with multislice image simulation and reconstructed the structure of Xe nanoclusters formed in Al crystalline matrix.

All of these examples illustrate the efficacy and power of Z-contrast imaging in HAADF-STEM for characterizing the occurrence of actinides and other heavy trace metals at near the atomic-scale, even at ppm levels of concentration. In particular, these examples provided new insight as to the form of migrating U and the other radionuclides in the environment. Another aspect is the importance of combination of the HAADF-STEM technique with the other state-of-the-art analytical methods: SIMS, TRLFS, and so on. Some of the examples show that multiparameter analysis combined with the STEM capability was still required for a complete understanding of the speciation of the element of interest, partly because of the limited volume of the TEM analysis and the relatively high level ( $\sim 0.1$  wt%) of detection limit in EDS (semi-) quantitative. However, recent developments in aberration correction in STEM has dramatically improved the capability of atomic-scale analysis and overcome some of the previous disadvantages. The advantages of  $C_S$ -corrected STEM are summarized in Sect. 5.



### 3 Electron Energy-Loss Spectroscopy

EELS with TEM is commonly used to determine the chemical state, such as the electronic structure of elements in target materials, in the small volume through which the electron beam passes. Fundamental aspects of EELS have been summarized in [57]. Application of EELS to the actinide research has been recently summarized in extensive reviews by Moore [58] and Moore and van der Laan [59]. As discussed by Moore [58] and Moore et al. [60], the EELS spectral shape is identical to synchrotron-based X-ray absorption spectrum. For actinide materials, several core-loss edges,  $O_{4,5}$  edge,  $N_{4,5}$  edge, and  $M_{4,5}$  edge, can be examined owing to the multiple shells of the electron orbitals. The  $O_{4,5}$  edge and  $N_{4,5}$  edge are shown in Fig. 9a, b [62, 63]. The  $O_{4,5}$  prepeak size and structure depend on the spin–orbit interaction of both the  $5d$  and  $5f$  states. In the case of the  $N_{4,5}$  edge, the ratio of the  $N_{4(d_{3/2})}$  and  $N_{5(d_{5/2})}$  peak intensities can be indicative of the relative occupation of the  $5f_{5/2}$  and  $5f_{7/2}$  levels.

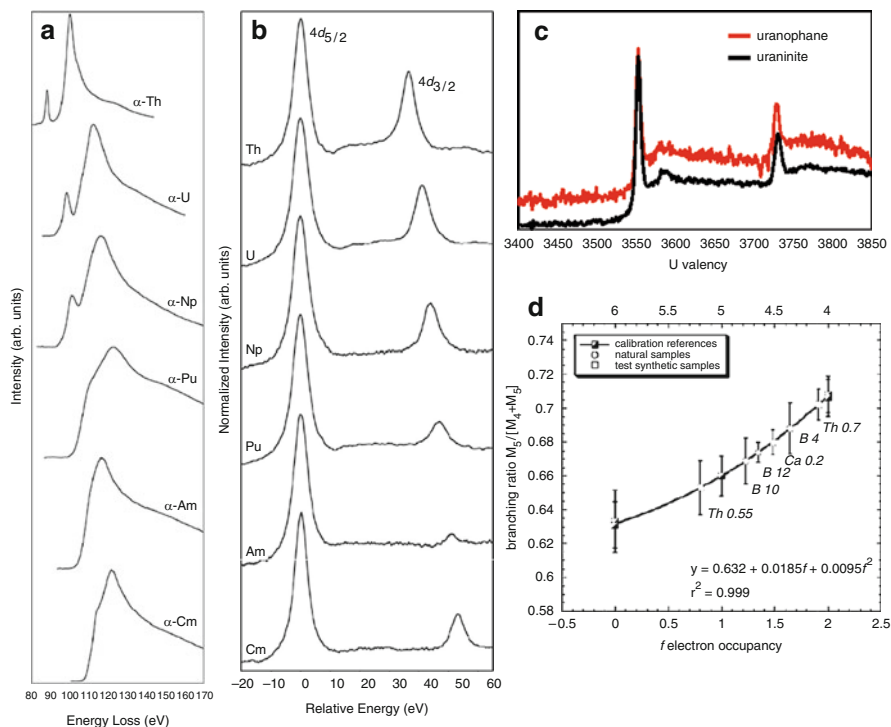


**Fig. 9** (a) The  $O_{4,5}$  ( $5d \rightarrow 5f$ ) EELS edges for the ground-state  $\alpha$ -phase of Th, U, Np, Pu, Am, and Cm metal. (b) The  $N_{4,5}$  ( $4d \rightarrow 5f$ ) EEL spectra for Th, U, Np, Pu, Am, and Cm metal. Each spectrum is normalized to the  $N_5$  peak height. (a) and (b) are from Moore and van der Laan [59]. (c) The  $M_{4,5}$  ( $3d \rightarrow 5f$ ) EEL spectra for synthetic uraninite,  $U(IV)O_2$ , and synthetic uranophane. (d) The correlation of the branching ratio  $M_5/(M_4+M_5)$  with the number of  $f$  electrons [61]

As in the EELS studies in nonradioactive elements [64, 65], a procedure to determine the chemical state of radionuclides by using EELS has been explored. A determination of the oxidation state of U at nanoscale is needed because the geochemical mobility of U varies as a function of its oxidation state. On the other hand,  $U^{5+}$  tends to disproportionate into  $U^{6+}$  and  $U^{4+}$ , except that relatively stable  $U^{5+}$  has been recognized on mineral surfaces; e.g., on the edge surface of biotite [66]. While X-ray photoelectron spectroscopy (XPS) and synchrotron-based X-ray absorption spectroscopy (XAS) have been widely used to quantify the oxidation state of U in experimentally prepared samples and natural samples, an analytical method at smaller scale than their probe size has been needed because the U frequently occurs localized in submicron domains. Naturally, EELS analysis of U has been attempted due to the high special resolution. Two EEL spectrums of U  $M_{4,5}$  edges taken from synthetic uraninite and synthetic uranophane are given in Fig. 9c as representative standards for  $U^{4+}$  and  $U^{6+}$ , respectively. As shown in the figure, these two spectra have minimum differences. Difficulties in determining U oxidation state are due to the low count in core-loss electrons at  $>3,000$  eV because the signal of EELS spectrum exponentially decreases as a function of energy and from electron beam-induced destruction of the structure with subsequent reduction of U oxidation state in many uranyl minerals. Colella et al. [61] have succeeded in determining U oxidation state using U  $M_{4,5}$  edge, of which the two white lines at 3,552 eV ( $M_5$ ), and 3,728 eV ( $M_4$ ) correspond to two electronic transitions  $3d_{5/2} - 5f_{7/2}$  and  $3d_{3/2} - 5f_{5/2}$ , respectively. The authors minimized the beam damage by keeping the specimen at the temperature of liquid nitrogen ( $-178^\circ\text{C}$ ) while using the maximized beam current to improve the signal to background ratio. The second derivative numerical filtering was applied to the spectra, and the integration of the peak intensity above zero was calculated in order to obtain the branching ratio,  $M_5/(M_4+M_5)$ , which polynomially correlates with the number of  $f$  electrons leading to the U valency (Fig. 9d). A similar method was applied to estimate the oxidation state of Pu [67]. The  $M_{4,5}$  edge was also used to detect ppm levels of actinides [68, 69].

## 4 Electron Tomography

### 4.1 Introduction of Electron Tomography by TEM

Electron tomography is a powerful method for obtaining the three-dimensional structure of various samples at the nanometer scale. Figure 10 shows an example of TEM three dimensional tomography, the reconstruction of an object viewed from different angles (Kamiishi and Utsunomiya, submitted). The specimen is hydroxyapatite reacted with 0.5 mM Pb nitrate solution for 9 h at room temperature. This three-dimensional reconstruction clearly reveals that Pb-hydroxyapatite precipitates and grows perpendicular to the  $c$ -axis only on the tip of the hydroxyapatite.



**Fig. 10** An example of electron tomography. The images are the ones tilted at  $0^\circ$  and  $\pm 54^\circ$  of BFTEM tomography. Hydroxypyromorphite nanocrystallite whisker and pseudomorph formed on hydroxyapatite are shown in three dimensions (Kamiishi and Utsunomiya, submitted). Full movie of BFTEM tomography is available on the web site (<http://mole.rc.kyushu-u.ac.jp/~ircl/>)

Tomography has been utilized in biological and physical sciences as an important technique for the study of the topology of biological materials, such as viruses or macromolecular assemblies. Their shape governs their specific chemical or physical properties. In material science, the use of tomography has been driven by the development of nanoscale devices.

Progress in tomographic reconstruction techniques has been accelerated by medical applications related to the development of the X-ray tomography in the (CT) scanner [70], which required new computational algorithms in order to construct the image. The method of tomography has been applied to many other disciplines including electron microscopy. In the early application of electron tomography, De Rosier and Klug [71] determined the three-dimensional structure of a biological macromolecule by the Fourier reconstruction methods, in which the helical symmetry of the structure allowed for reconstruction from a single projection. Later, Hoppe et al. [72] demonstrated that reconstruction from multiple projections is possible for asymmetrical systems.

## 4.2 Data Collection and Reconstruction

Data for electron tomography can be obtained by tilting the specimen with respect to the electron beam. In general, a tilt series is taken at  $1\text{--}2^\circ$  angular intervals over an angle range of  $-60^\circ$  to  $+60^\circ$  using specially designed high-tilt specimen holder. This holder is modified by reducing the width of the holder to minimize the effect of shadowing of the specimen by the holder edge. The resolution and quantity of the reconstructed object depend on the angular range and the angular step of the tilt, as well as the resolution of the projections. The acquired projections must be corrected by estimating the sample movement based on the FFT cross-correlation. In most

cases, reconstruction in electron tomography is carried out by back-projection procedure, in which a tilt series of the projected BFTEM or HAADF-STEM images were utilized to build the three dimensional structure. The procedure in electron tomography is concisely described in Midgley and Weyland [73]. Briefly, a point in space may be uniquely described by any three rays passing through that point. If the shape of an object is complex, more rays are then required to describe it uniquely. Fundamentally, a projection of an object is an inverse of such a ray, and will describe some of the complexity of that object. Therefore, inverting the projection, “smearing out” the projection into an object space at the angle of projection, generates a ray that will describe uniquely an object in the projection direction.

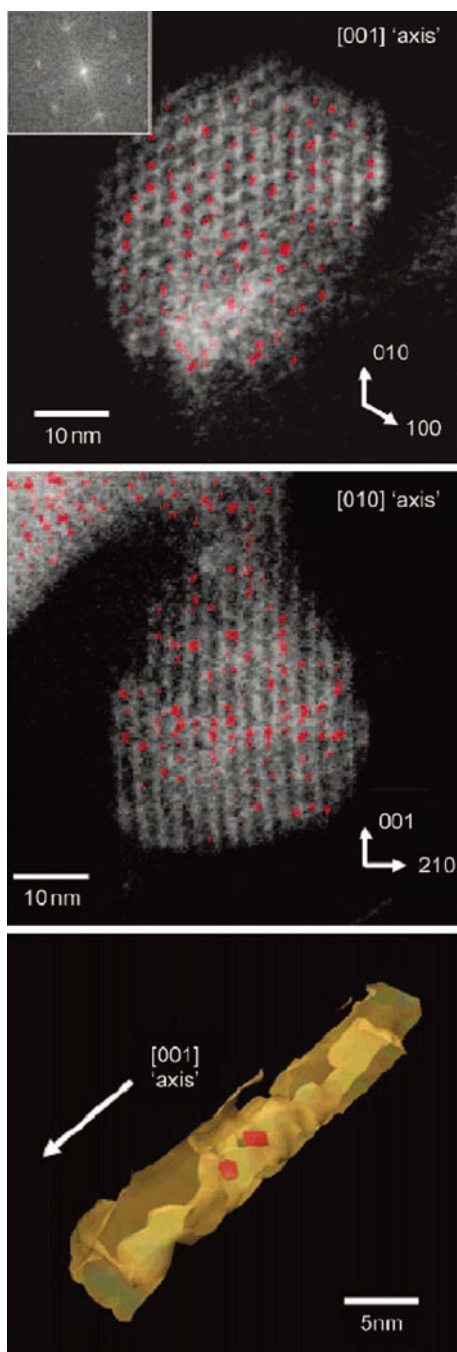
### ***4.3 Application of HAADF-STEM and Energy-Filtered TEM to Electron Tomography***

Most of the previous electron tomography studies are reconstructed from a tilt series of BF-TEM images. In the case of a noncrystalline specimen, the contrast of BF image is correlated with thickness and density of the target. However, for crystalline materials, the contrast depends on the diffraction condition of the crystal, resulting in BF images of this case being less suitable for the tomographic reconstruction [74]. Therefore, application of HAADF-STEM and energy-filtered TEM (EFTEM) to tomography has been recently explored in the physical sciences. As an example, a heterogeneous catalyst composed of Pd<sub>6</sub>Ru<sub>6</sub> particles (~1 nm in diameter) within a mesoporous silica was located using this technique [75]. The authors were able to show evidence of a single Pd<sub>6</sub>Ru<sub>6</sub> particle anchored to the wall of the mesopore (Fig. 11). In addition, by using a tilt series of EFTEM elemental maps, it is possible to reconstruct a three-dimensional elemental distribution map [76, 77].

### ***4.4 Prospect of Electron Tomography in Actinide Research***

Applications of electron tomography continue to expand. A new technique for acquiring a complete tilt series (tilt angular range:  $\pm 90^\circ$ ) of a specimen can eliminate the missing tilt angle, which is created in the shadow zone by the holder edge [78]. Aberration-corrected STEM allows the reconstruction of high-resolution atomic-scale tomography by varying the probe focusing point rather than tilting sample [79, 80]. Although the application of electron tomography has not been explored in actinide research, this technique should be a powerful approach to the investigation of the three dimensional distribution, topology, and orientation of actinide nanoparticles, nanodomains, and even single atoms.

**Fig. 11** Three-dimensional structure of an heterogeneous catalyst composed of  $\text{Pd}_6\text{Ru}_6$  particles, colored *red*, within a mesoporous silica support (MCM-41). (a) and (b): two perpendicular voxel projections of the reconstruction volume. (c) A surface render of a single mesopore extracted from the volume to reveal two nanoparticles within its interior [75]



## 5 Aberration-Corrected STEM

Recently, the resolution of STEM, as well as TEM, has dramatically improved due to the revolutionary development of aberration correction technology. The achievement of ultra-high resolution is due to the correction of spherical aberration ( $C_S$ ). Resolution of  $C_S$ -corrected STEM now achieved single atomic column or single atom scale. The  $C_S$ -corrected STEM and TEM in conjunction with EELS, EDS, and HAADF detector allow us to perform multiparameter analysis with better resolution and quality than the conventional STEM and TEM. This section is intended to concisely summarize several aspects related to  $C_S$ -corrected STEM based on its potential for application to actinide research.

### 5.1 Basics of $C_S$ Corrector

The  $C_S$  stands for the spherical aberration of rotationally electromagnetic lenses. Spherical aberration was discovered, with chromatic aberration ( $C_C$ ) as the unavoidable aberration of rotationally electromagnetic lenses [81]; these aberrations cause image blurring and limit the spatial resolution to about 2 Å, which is 50 times the wavelength of electrons accelerated in 100–200 keV. Spherical aberration mainly causes this blurring, and the resolution limit  $d$  is expressed by  $d = AC_S^{1/4}\lambda^{3/4}$  ( $A \approx 0.66$ ) [82, 83], where  $A$  is the constant that depends on the condition of microscope,  $C_S$  is the spherical aberration coefficient, and  $\lambda$  is the wavelength of the electron. From this equation, it is evident that reducing the value of  $C_S$  can lead to an improvement in the resolution. The schematic illustration of spherical aberration and correction by multipole corrector is shown in Fig. 12 [85].

### 5.2 The History of $C_S$ Correction

Since Scherzer [81] pointed out that rotationally symmetric electron lenses of transmission electron microscope have unavoidable aberrations and proposed some alternative ways to improve the resolution by correcting aberrations, many researchers have tried to compensate for the aberration, and  $C_S$ -corrected TEM (not STEM) developed with greatly improved resolution in the early 1990s [84, 86].

On the other hand, after the invention of STEM in the late 1960s as a novel alternative technique to the TEM imaging [87], researchers started to correct aberrations in STEM in the early 1970s, and considerable effort to correct the aberration had been made over the last 40 years [88]. This effort led to the development of aberration corrector to compensate for the spherical aberration: hexapole corrector [89–91], quadrupole–octopole corrector, and multipole corrector [92, 93]. A series of articles [94, 95] reported the progress in the development of

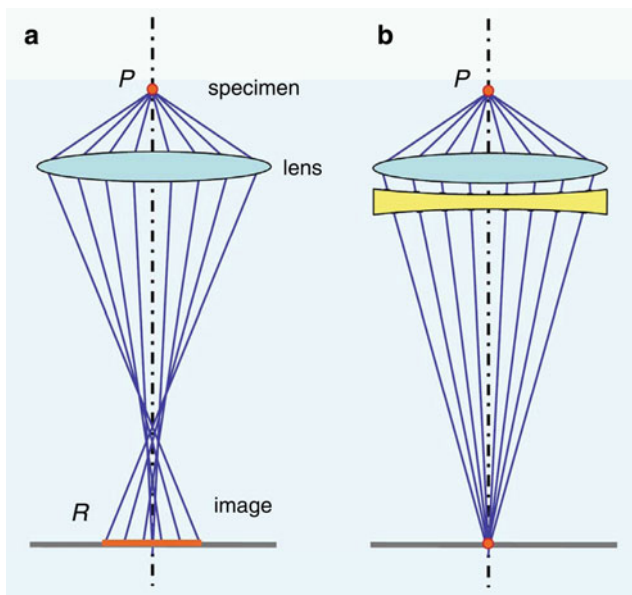


**Fig. 12** The schematic illustration of spherical aberration and correction by multipole corrector [84]. (a) Spherical aberration of a converging lens. The focal length of the electron beams passing outside of the lens form a focal point distance in front of the image plane that is defined by the paraxial beams. The image of point  $P$  is blurred and imaged as disk of radius  $R$  on the plane. (b) Aberration corrector combined with the lens compensates the spherical aberration

aberration corrector implemented in VG dedicated STEM. By 2003, when the articles were written, a sub- $\text{\AA}$  sized electron probe and the current of an atom-sized probe by a factor of more than 10 had been achieved. The resolution limit of TEM and STEM is currently achieved at  $0.5 \text{ \AA}$  due to the simultaneous correction of the chromatic aberration and spherical aberration using multipole correctors, and improvement of mechanical stability in the framework of the transmission electron aberration-corrected microscope (TEAM) project that was initiated in the early 2000s [96]. The historical progress in resolution of microscopes is illustrated in Fig. 13 [98].

### 5.3 Merit and Application of $C_S$ -Corrected STEM

At first, one can simply observe and characterize individual atoms with high sensitivity, because the high beam current created by using  $C_S$ -corrector allows one to obtain strong signals in imaging and analysis [97, 99]. In addition,  $C_S$ -corrected STEM can achieve the sub- $\text{\AA}$  resolution even at low voltage, thus minimizing damage to the specimen. Hence, some beam-sensitive materials consisting of light elements have been observed recently, such as monolayer BN [10].

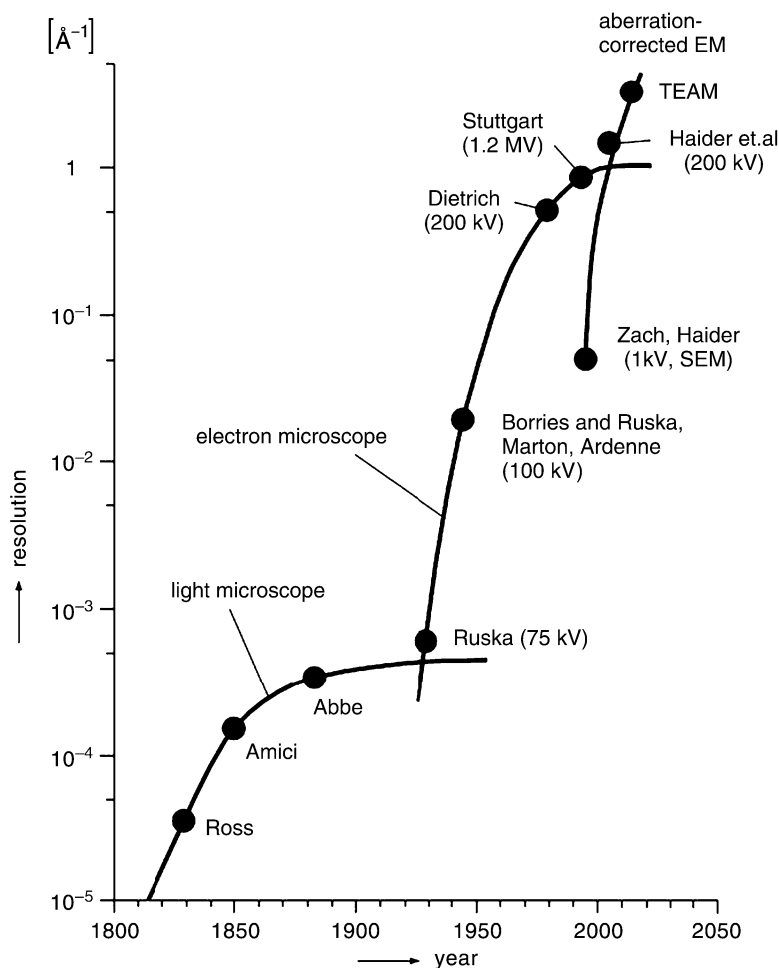


**Fig. 13** The historical progress in the resolution of electron microscopes [97]

The focus of current research using  $C_s$ -corrected STEM is not only on the light element compounds but also on the analysis of heavy metals such as Au atoms and their behavior on amorphous carbon [97, 100].

#### 5.4 Atomic-Resolution Spectroscopic Imaging

Coinciding with the great improvement in probe size and electron current in STEM, atomic-resolution spectroscopic imaging has greatly advanced in materials research. As a further application, the technique of aberration-corrected STEM in conjunction with EELS has allowed column-by-column resolution analysis of



chemical composition, electronic structure, and oxidation state analysis [101–103]. Interestingly, Varela et al. [103] have also demonstrated different methods for obtaining the average oxidation state of Mn in manganite and concluded that the O K edge  $\Delta E$  (main peak to pre-peak separation) method is the most reliable. In some special cases, chemical analysis at the atom-by-atom level has succeeded [10, 99, 104, 105]. Nevertheless, a caution was raised by Oxley et al. [106] concerning the factors that affect the contrast of atomic-resolution spectroscopic image. Specimen thickness is a particularly important parameter that can potentially modify the EELS image due to a dechanneling phenomenon, in which the heavier elements scatter electrons at higher angle, lowering the number of electrons in the EELS image [106, 107]. As a result, the spectroscopic image simulation is necessary for detailed investigation at the sub Å scale when the specimen thickness becomes thicker than  $\sim 100$  Å. Further aspects in terms of development in spectroscopic imaging using  $C_S$ -STEM have been reviewed in Pennycook et al. [107].

## 5.5 Future Developments

A sub Å electron probe formed by  $C_S$  corrector has made it possible to perform multiparameter analysis at the sub Å level. Although the application of  $C_S$ -corrected STEM to nuclear science has never been explored, such a capability will have a great impact on our ability to investigate nuclear materials, because the atomic-scale phenomena are closely linked to bulk properties. As mentioned in Pennycook et al. [107], “the intrinsic benefits of STEM for simultaneous imaging of atomic and electronic structure have progressed from a dream limited by noise to a practical reality waiting for application”. Still, it is easy to imagine that the resolution limit will be further improved in future with progress in the development of aberration correctors.

**Acknowledgments** The authors acknowledge the staff of the high voltage electron microscopy (HVEM) laboratory at Kyushu University for their technical support and daily maintenance. SU also thanks the members of the nanogeoscience group in the Department of Chemistry at Kyushu University for their help and constructive discussion. R.C. Ewing acknowledges support from the Energy Frontier Research Center, Materials Science of Actinides, funded by the U.S. Department of Energy, Office of Science, Basic Energy Sciences under Award Number DE-SC0001089.

## References

1. Lutze W, Malow G, Ewing RC, Jercinovic MJ, Keil K (1985) Alteration of basalt glasses: Implications for modelling the long-term stability of nuclear waste glasses. *Nature* 314:252–255
2. Murakami T, Ewing RC, Bunker BC (1988) Analytical electron microscopy of leached layers on synthetic basalt glass. In: Apted MJ and Westerman RE (eds) *Scientific Basis for Nuclear Waste Management XI*. *Mater Res Soc Proc* 112:737–748

3. Murakami T, Jercinovic MJ, Ewing RC (1989) Formation and evolution of alteration layers of borosilicate and basaltic glasses I: Initial stage. In: Lutze W, Ewing RC (eds) *Scientific Basis for Nuclear Waste Management XII*. Mater Res Soc Proc 127:65–72
4. Bates JK, Bradley JP, Teetsov A, Bradley CR, Tenbrink MB (1992) Colloid formation during waste form reaction: implications for nuclear waste disposal. *Science* 256:649–651
5. Thomas LE, Beyer CE, Charlot LA (1992) Microstructural analysis of LWR spent fuels at high burnup. *J Nucl Mater* 188:80–89
6. Williams DB, Carter CB (1996) *Transmission electron microscopy. A Textbook for Materials Science*. Springer, New York
7. Fultz B, Howe JM (2007) *Transmission Electron Microscopy and Diffractometry of Materials*, 3rd edition. Springer, New York
8. Kirkland EJ (1998) *Advanced Computing in Electron Microscopy*, 1st edition. Plenum Press, New York
9. Utsunomiya S, Ewing RC (2003) Application of high-angle annular dark field scanning transmission electron microscopy, scanning transmission electron microscopy-energy dispersive X-ray spectrometry, and the energy-filtered transmission electron microscopy to the characterization of nanoparticles in the environment. *Environ Sci Technol* 37:786–791
10. Krivanek OL, Chisholm MF, Nicolosi V, Pennycook TJ, Corbin GJ, Dellby N, Murfitt MF, Own CS, Szilagyi ZS, Oxley MP, Pantelides ST, Pennycook SJ (2010) Atom-by-atom structural and chemical analysis by annular dark-field electron microscopy. *Nature* 464:571–574
11. Crewe AV, Wall J, Langmore J (1970) Visibility of single atoms. *Science* 168:1338–1340
12. Isaacson M, Kopf D, Ohtsuki M, Utlaut M (1979) Atomic imaging using the dark-field annular detector. *Ultramicroscopy* 4:101–104
13. Liu J, Cowley JM (1990) High-angle ADF and high-resolution SE imaging of supported catalyst clusters. *Ultramicroscopy* 34:119–128
14. Pennycook SJ (1989) Z-contrast STEM for materials science. *Ultramicroscopy* 30:58–69
15. Pennycook SJ, Boatner LA (1988) Chemically sensitive structure-imaging with a scanning transmission electron microscope. *Nature* 336:565–567
16. Chisholm MF, Pennycook SJ (2006) Direct imaging of dislocation core structures by Z-contrast STEM. *Philos Mag* 86:4699–4725
17. Wang ZL, Cowley JM (1989) Simulating high-angle annular dark-field STEM images including inelastic thermal diffuse scattering. *Ultramicroscopy* 31:437–454
18. Pennycook SJ, Jesson DE (1991) High-resolution incoherent imaging of crystals. *Phys Rev Lett* 64:938–941
19. Treacy MMJ, Gibson JM (1993) Coherence and multiple scattering in “Z-contrast” images. *Ultramicroscopy* 52:31–53
20. Hillyard S, Loane RF, Silcox J (1993) Annular dark-field imaging: resolution and thickness effects. *Ultramicroscopy* 49:14–25
21. Yamazaki T, Watanabe K, Recnik A, Ceh M, Kawasaki M, Shiojiri M (2000) Simulation of atomic-scale high-angle annular dark field scanning transmission microscopy images. *J Electron Microsc* 49:753–759
22. Kirkland EJ, Loane RF, Silcox J (1987) Simulation of annular dark field stem images using a modified multislice method. *Ultramicroscopy* 23:77–96
23. Stadelmann PA (1987) EMS – A software package for electron diffraction analysis and HREM image simulation in materials science. *Ultramicroscopy* 21:131
24. Ishizuka K (2002) A practical approach for STEM image simulation based on the FFT multislice method. *Ultramicroscopy* 90:71–83
25. McGibbon AJ, Pennycook SJ, Jesson DE (1999) Crystal structure retrieval by maximum entropy analysis of atomic resolution incoherent images. *J Microsc* 195:44–57
26. Gull SF, Skilling J (1984) Maximum entropy method in image processing. *IEE Proc* 131:646–659

27. Gull SF (1989) Developments in maximum entropy data analysis. In Maximum Entropy and Bayesian Methods. Skilling J (ed) 53–71 Kluwer Academic, Boston
28. Chisholm MF, Pennycook SJ (1991) Structural origin of reduced critical currents at  $\text{YBa}_2\text{Cu}_3\text{O}_{7-\delta}$  grain boundaries. *Nature* 351:47–49
29. Utsunomiya S, Jensen KA, Keeler GJ, Ewing RC (2002) Uraninite and fullerene in atmospheric particulates. *Environ Sci Technol* 36:4943–4947
30. Lovley DR, Phillips EJP, Gorby YA, Landa ER (1991) Microbial reduction of uranium. *Nature* 350:413–416
31. Abdelouas A, Lutze W, Nuttall HE (1999) Uranium contamination in the subsurface: characterization and remediation. In: Burns PC and Finch R (eds) *Uranium: Mineralogy, Geochemistry and the Environment*. Mineral Soc Am 38:433–473
32. Suzuki Y, Banfield JF (1999) Geomicrobiology of uranium. In: Burns PC and Finch RJ (eds) *Uranium: Mineralogy, Geochemistry and the Environment*. *Rev Miner* 38:393–432
33. Suzuki Y, Kelly SD, Kemner KM, Banfield JF (2002) Nanometre-size products of uranium bioreduction. *Nature* 419:134
34. Fayek M, Utsunomiya S, Pfiffner SM, Anovitz L, White DC, Riciputi LR, Ewing RC, Stadermann FJ (2005) Predicting the stability of nano-scale bio-precipitated uranium phases. *Can Mineral* 43:1631–1641
35. Finch RJ, Murakami T (1999) Systematics and paragenesis of uranium minerals. In: Burns PC and Finch RJ (eds) *Uranium: Mineralogy, Geochemistry and the Environment*. *Rev Miner Geochem* 38:91–179
36. Deditius AP, Utsunomiya S, Ewing RC (2008) The chemical stability of coffinite,  $\text{USiO}_4 \cdot n\text{H}_2\text{O}$ ;  $0 < n < 2$ , associated with organic matter: A case study from Grants uranium region, New Mexico, USA. *Chem Geol* 251:33–49
37. Deditius AP, Utsunomiya S, Poiteau V, Ewing RC (2010) Precipitation and alteration of coffinite ( $\text{USiO}_4 \cdot n\text{H}_2\text{O}$ ) in the presence of apatite. *Eur J Mineral* 22:75–88
38. Deditius AP, Utsunomiya S, Wall MA, Poiteau V, Ewing RC (2009) Crystal chemistry and radiation-induced amorphization of P-coffite from the natural fission reactor at Bangonbé, Gabon. *Am Mineral* 94:827–836
39. McCarthy JF, Zachara JM (1989) Subsurface transport of contaminants-mobile colloids in the subsurface environment may alter the transport of contaminants. *Environ Sci Technol* 23:496–502
40. Kim JI (1994) Actinide colloids in natural aquifer systems. *Mater Res Soc Bull* 19:47–53
41. Kim JI (1993) The chemical behavior of transuranium elements and barrier functions in natural aquifer systems. *Mater Res Soc Symp Proc* 294:3–21
42. Utsunomiya S, Kersting AB, Ewing RC (2009) Groundwater nanoparticles in the far-field at the Nevada test site: mechanism for radionuclide transport. *Environ Sci Technol* 43:1293–1298
43. Novikov AP, Kalmykov SN, Utsunomiya S, Ewing RC, Horreard F, Merkulov A, Clark SB, Tkachev VV, Myasoedov BF (2006) Colloid transport of plutonium in the far-field of the Mayak Production Association, Russia. *Science* 314:638–641
44. Kersting AB, Efurd DW, Finnegan DL, Rokop DJ, Smith DK, Thompson JL (1999) Migration of plutonium in groundwater at the Nevada Test Site. *Nature* 397:56–59
45. Arnold T, Utsunomiya S, Geipel G, Ewing RC, Baumann N, Brendler V (2006) Adsorbed U (VI) surface species on muscovite by TRLFS and HAADF-STEM. *Environ Sci Technol* 40:4646–4652
46. Ilton ES, Haiduc A, Moses CO, Heald SM, Elbert DC, Veblen DR (2004) Heterogeneous reduction of uranyl by micas: crystal chemical and solution controls. *Geochim Cosmochim Acta* 68:2417–2435
47. Ewing RC, Lutze W, Weber WJ (1995) Zircon: a host-phase for the disposal of weapons plutonium. *J Mater Res* 10:243–246
48. Ewing RC (1999) Nuclear waste forms for actinides. *Proc Natl Acad Sci USA* 96:3432–3439

49. Utsunomiya S, Palenik CS, Valley JW, Cavosie AJ, Wilde SA, Ewing RC (2004) Nanoscale occurrence of Pb in an Archean zircon. *Geochim Cosmochim Acta* 68:4679–4686
50. Valley JW (2003) Oxygen isotopes in Zircon. In: Hanchar J (ed) *Zircon*. Mineralogical Society of America, Washington, DC. *Rev Mineral Geochem* 53:343–385
51. Wilde SA, Valley JW, Peck WH, Graham CM (2001) Evidence from detrital zircons for the existence of continental crust and oceans on the Earth 4.4 Gyr ago. *Nature* 409:175–178
52. Utsunomiya S, Ewing RC (2006) The fate of the epsilon phase (Mo-Ru-Pd-Tc-Rh) in the UO<sub>2</sub> of the Oklo natural fission reactors. *Radiochim Acta* 94:749–753
53. Utsunomiya S, Yudinsev S, Ewing RC (2005) Radiation effects of ferrate garnet. *J Nucl Mater* 336:251–260
54. Weber WJ (1991) Self-radiation damage and recovery in Pu-doped zircon. *Radiat Effect Defects Solids* 115:341–349
55. Weber WJ, Ewing RC, Wang LM (1994) The radiation-induced crystalline-to-amorphous transition in zircon. *J Mater Res* 9:688–698
56. Mitsuishi K, Kawasaki M, Takeguchi M, Yasuda H, Furuya K (2001) High-angle annular dark-field STEM observation of Xe nanocrystals embedded in Al. *Ultramicroscopy* 88:25–31
57. Egerton RF (1996) *Electron Energy-Loss Spectroscopy in the Electron Microscope*, 2nd edition. Plenum, New York
58. Moore KT (2010) X-ray and electron microscopy of actinide materials. *Micron* 41:336–358
59. Moore KT, van der Laan G (2009) Nature of the 5f states in actinide metals. *Rev Mod Phys* 81:235–298
60. Moore KT, Chung BW, Morton SA, Schwartz AJ, Tobin JG, Lazar S, Tichelaar FD, Zandbergen HW, Soderlind P, van der Laan G (2004) Changes in the electronic structure of cerium due to variations in close packing. *Phys Rev B* 69:193104
61. Colella M, Lumpkin GR, Zhang Z, Buck EC, Smith KL (2005) Determination of the uranium valence state in the brannerite structure using EELS, XPS, and EDX. *Phys Chem Min* 32:52–64
62. Butterfield MT, Moore KT, van der Laan G, Wall MA, Haire RG (2008) Understanding the O<sub>4,5</sub> edge structure of actinide metals: Electron energy-loss spectroscopy and atomic spectral calculations of Th, U, Np, Pu, Am, and Cm. *Phys Rev B* 77:113109
63. Moore KT, van der Laan G, Wall MA, Schwartz AJ, Haire RG (2007) Rampant changes in 5f<sub>5/2</sub> and 5f<sub>7/2</sub> filling across the light and middle actinide metals: Electron energy-loss spectroscopy, many-electron atomic spectral calculations, and spin-orbit sum rule. *Phys Rev B* 76:073105
64. Garvie LAJ, Buseck PR (1998) Ferrous/ferric ratios from nanometer-sized areas in minerals. *Nature* 396:667–670
65. Garvie LAJ, Buseck PR (1999) Determination of Ce<sup>4+</sup>/Ce<sup>3+</sup> in electron-beam-damaged CeO<sub>2</sub> by electron energy-loss spectroscopy. *J Phys Chem Solids* 60:1943–1947
66. Ilton ES, Haiduc A, Cahill CL, Felmy AR (2005) Mica surfaces stabilize pentavalent uranium. *Inorg Chem* 44:2986–2988
67. Buck EC, Finn PA, Bates JK (2004) Electron energy-loss spectroscopy of anomalous plutonium behavior in nuclear waste materials. *Micron* 35:235–243
68. Buck EC, Bates JK (1999) Microanalysis of colloids and suspended particles from nuclear waste glass alteration. *Appl Geochem* 14:635–653
69. Buck EC, Douglas M, Wittman RS (2010) Verifying the presence of low levels of neptunium in a uranium matrix with electron energy-loss spectroscopy. *Micron* 41:65–70
70. Cormack AM (1963) Representation of a function by its line integrals with some radiological applications. *J Appl Phys* 34:2722–2727
71. De Rosier DJ, Klug A (1968) Reconstruction of three dimensional structures from electron micrographs. *Nature* 217:130–134
72. Hoppe W, Langer R, Knesch G, Poppe C (1968) Protein crystal structure analysis with electron rays. *Naturwissenschaften* 55:333

73. Midgley PA, Weyland M (2003) 3D electron microscopy in the physical science: the development of Z-contrast and EFTEM tomography. *Ultramicroscopy* 96:413–431
74. Friedrich H, McCartney MR, Buseck PR (2005) Comparison of intensity distributions in tomograms from BFTEM, ADF STEM, HAADF STEM, and calculated tilt series. *Ultramicroscopy* 106:18–27
75. Midgley PA, Thomas JM, Laffont L, Weyland M, Raja R, Johnson BFG, Khimyak T (2004) High-resolution scanning transmission electron tomography and elemental analysis of zeptomogram quantities of heterogeneous catalyst. *J Phys Chem B* 108:4590–4592
76. Mobus G, Inkson BJ (2001) Three-dimensional reconstruction of buried nanoparticles by element sensitive tomography based on inelastically scattered electrons. *Appl Phys Lett* 79:1369–1371
77. Weyland M, Midgley PA (2003) Extending energy-filtered transmission electron microscopy (EFTEM) into three dimensions using electron tomography. *Microsc Microanal* 9:542–555
78. Kawase N, Kato M, Nishioka H, Jinnai H (2007) Transmission electron microtomography without the “missing wedge” for quantitative structural analysis. *Ultramicroscopy* 107:8–15
79. Sadan MB, Houben L, Wolf SG, Enyashin A, Seifert G, Tenne R, Urban K (2008) Toward atomic-scale bright-field electron tomography for the study of fullerene-like nanostructures. *Nano Lett* 8:891–896
80. Xin HL, Muller DA (2009) Aberration-corrected ADF-STEM depth sectioning and prospects for reliable 3D imaging in S/TEM. *J Electron Microsc* 58:157–165
81. Scherzer O (1949) The theoretical resolution limit of the electron microscope. *J Appl Phys* 20:20–29
82. Cowley JM (1976) Scanning transmission electron microscopy of thin specimens. *Ultramicroscopy* 2:3–16
83. Smith DJ (2008) Development of aberration-corrected electron microscopy. *Microsc Microanal* 14:2–15
84. Haider M, Rose H, Uhlemann S, Kabius B, Urban K (1998) Towards 0.1 nm resolution with the first spherically corrected transmission electron microscope. *J Electron Microsc* 47:395–405
85. Urban K (2008) Studying atomic structures by aberration-corrected transmission electron microscopy. *Science* 321:506–510
86. Haider M, Uhlemann S, Schwan E, Rose H, Kabius B, Urban K (1998) Electron microscopy image enhanced. *Nature* 392:768–769
87. Crewe AV, Isaacson M, Johnson D (1969) A simple scanning electron microscope. *Rev Sci Instrum* 40:241–246
88. Crewe AV (2004) Some Chicago aberrations. *Microsc Microanal* 10:414–419
89. Beck VD (1979) A hexapole spherical aberration corrector. *Optik* 53:241–255
90. Crewe AV (1980) Studies on sextupole correctors. *Optik* 57:313–327
91. Rose H (1981) Correction of aperture aberrations in magnetic systems with threefold symmetry. *Nucl Instrum Methods* 187:187–199
92. Zach J (1989) Design of a high-resolution low-voltage scanning electron microscope. *Optik* 83:30–40
93. Zach J, Haider M (1995) Aberration correction in a low-voltage SEM by a multipole corrector. *Nucl Instrum Methods A* 365:316–325
94. Krivanek OL, Dellby N, Lupini AR (1999) Towards sub-Å electron beams. *Ultramicroscopy* 78:1–11
95. Krivanek OL, Nellist PD, Dellby N, Murfitt MF, Szilagy Z (2003) Towards sub-0.5 Å electron beams. *Ultramicroscopy* 96:229–237
96. Rose H (2005) Prospects for aberration-free electron microscopy. *Ultramicroscopy* 103:1–6
97. Batson PE, Dellby N, Krivanek OL (2002) Sub-angstrom resolution using aberration corrected electron optics. *Nature* 418:617–620
98. Rose H (2009) Historical aspects of aberration correction. *J Electron Microsc* 58:77–85

99. Muller DA, Kourkoutis LF, Murfitt M, Song JH, Hwang HY, Silcox J, Dellby N, Krivanek OL (2008) Atomic-scale chemical imaging of composition and bonding by aberration-corrected microscopy. *Science* 319:1073–1076
100. Batson PE (2008) Motion of gold atoms on carbon in the aberration-corrected STEM. *Microsc Microanal* 14:89–97
101. Pennycook SJ, Jesson DE, Browning ND (1995) Atomic-resolution electron energy loss spectroscopy in crystalline solids. *Nucl Instrum Methods B* 96:575–582
102. Browning ND, Wallis DJ, Nellist PD, Pennycook SJ (1997) EELS in the STEM: determination of materials properties on the atomic scale. *Micron* 28:333–348
103. Varela M, Oxley MP, Luo W, Tao J, Watanabe M, Lupini AR, Pantelides ST, Pennycook SJ (2009) Atomic-resolution imaging of oxidation states in manganites. *Phys Rev B* 79:085117
104. Crewe AV, Isaacson M, Johnson D (1971) A high resolution electron spectrometer for use in transmission scanning electron microscopy. *Rev Sci Instrum* 42:411–420
105. Batson PE (1993) Simultaneous STEM imaging and electron energy-loss spectroscopy with atomic-column sensitivity. *Nature* 366:727–728
106. Oxley MP, Varela M, Pennycook TJ, van Benthem K, Findlay SD, D'Alfonso AJ, Allen LJ, Pennycook SJ (2007) Interpreting atomic-resolution spectroscopic images. *Phys Rev B* 76:064303
107. Pennycook SJ, Varela M, Lupini AR, Oxley MP, Chisholm MF (2009) Atomic-resolution spectroscopic imaging: past, present and future. *J Electron Microsc* 58:87–97

Actinide Nanoparticle Research

Kalmykov, S.N.; Denecke, M.A. (Eds.)

2011, XIX, 440 p., Hardcover

ISBN: 978-3-642-11431-1